

## A stiff scanning tunneling microscopy head for measurement at low temperatures and in high magnetic fields

S. C. White, U. R. Singh, and P. Wahl

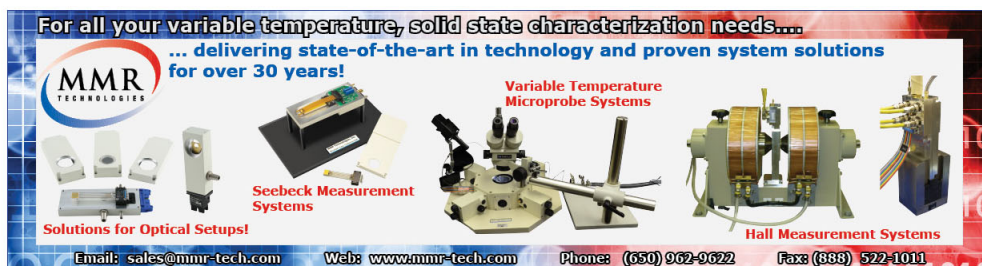
Citation: [Review of Scientific Instruments](#) **82**, 113708 (2011); doi: 10.1063/1.3663611

View online: <http://dx.doi.org/10.1063/1.3663611>

View Table of Contents: <http://scitation.aip.org/content/aip/journal/rsi/82/11?ver=pdfcov>

Published by the [AIP Publishing](#)

---



For all your variable temperature, solid state characterization needs....  
... delivering state-of-the-art in technology and proven system solutions  
for over 30 years!

**MMR**  
TECHNOLOGIES

**Seebeck Measurement Systems**

**Variable Temperature Microprobe Systems**

**Hall Measurement Systems**

Solutions for Optical Setups!

Email: [sales@mmr-tech.com](mailto:sales@mmr-tech.com) Web: [www.mmr-tech.com](http://www.mmr-tech.com) Phone: (650) 962-9622 Fax: (888) 522-1011

## A stiff scanning tunneling microscopy head for measurement at low temperatures and in high magnetic fields

S. C. White, U. R. Singh, and P. Wahl

*Max-Planck-Institut für Festkörperforschung, Heisenbergstr. 1, D-70569 Stuttgart, Germany*

(Received 30 June 2011; accepted 2 November 2011; published online 29 November 2011)

We have developed a measurement head for scanning tunneling microscopy (STM) and specifically for spectroscopic imaging STM which is optimized for high mechanical stiffness and good thermal conductivity by choice of material. The main components of the microscope head are made of sapphire. Sapphire has been chosen from several competing possibilities based on finite element modeling of the fundamental vibrational modes of the body. We demonstrate operation of the STM head in topographic imaging and tunneling spectroscopy at temperatures down to below 2 K. © 2011 American Institute of Physics. [doi:10.1063/1.3663611]

The investigation of the electronic structure of correlated electron systems by spectroscopic imaging scanning tunneling microscopy (SI-STM) has in the past years become an increasingly active field of research. Since it provides information on both local inhomogeneities and the properties of single defects,<sup>1</sup> as well as a look at the band structure in the vicinity of the Fermi level,<sup>2,3</sup> SI-STM has proven itself an especially valuable tool for studying the physics of correlated electron materials – which is often influenced by interactions between localized and delocalized electron states. STM is unique, in part, because it allows the simultaneous characterization of electronic states in both real space and momentum space.<sup>4</sup> Unfortunately, extreme requirements on the stability of the tip-sample junction, which necessitate extensive external vibration isolation, have for the most part limited this technique to labs with dedicated low-vibration facilities. In order to improve the intrinsic stability of the tunneling junction and relax the required complexity of external vibration isolation, we have developed an STM measurement head with high frequency resonant modes.<sup>5,6</sup> Tuning the frequency of the fundamental modes ( $\omega_r$ ) is an effective strategy for improving the instrument's intrinsic stability because of the limits they impose on external disruptions to the tunneling junction due to mechanical vibrations. The effect, on an STM measurement head, of external vibrations with frequencies lower than resonance ( $\omega < \omega_r$ ) will be strongly suppressed as the tip and sample move in phase, while frequencies greater than the resonance frequency ( $\omega > \omega_r$ ) will be fully transmitted to the tunneling junction. Therefore, it is helpful to increase the frequency of the instruments fundamental resonant modes as much as possible. An increase of the resonance frequency of the STM head by a factor of two reduces the transmission of perturbations in the low frequency range ( $\omega \ll \omega_r$ ) by a factor of four. One way to achieve increased fundamental resonance frequencies is to optimize the geometry.<sup>7</sup> We have achieved increased mechanical stiffness primarily by optimizing the choice of materials – the geometric architecture<sup>8</sup> has not been significantly altered. Microscopic and spectroscopic operation is demonstrated with the new STM head in a cryogenic environment.

In this STM design, the coarse approach of the tip towards the sample (from below) is realized through a flattened V-shaped cavity in which a prism is clamped between six piezo stacks.<sup>9</sup> By laterally actuating the piezo stacks, the central prism can be moved up or down. Due to its compact and rigid form, this STM design provides a high level of stability.<sup>10</sup> To optimize the mechanical stiffness of the measurement head and hence further improve stability, we first performed finite element calculations to obtain the fundamental vibrational modes of the modeled head for three possible materials.<sup>11</sup> We gave preference to non-conducting materials in order to reduce the risk of electrical shorts, as well as to make the head less susceptible to possible heating from eddy currents (while ramping the magnetic field). We have performed the calculations for the four lowest frequency modes; the mesh used as well as the resulting displacement and stress patterns are depicted in Fig. 1. The results for MACOR, amorphous aluminum oxide, and sapphire are summarized in Table I. We found that among the different materials, the resonant mode frequencies of the simulated STM head – which scale with  $\sqrt{G/\rho}$  – vary by almost a factor of two. Based on the calculations, we chose to build our STM head from oriented single-crystalline sapphire. In addition to having the highest level of stiffness, sapphire also has a very good thermal conductivity,<sup>12</sup> e.g., much better than that of MACOR. Short thermalization times with cessation of related drift effects can, thus, be achieved. Furthermore, by using the same material (sapphire) for both the main body components (the slider and the frame) and molybdenum for other structural components, stress effects due to differing coefficients of thermal expansion are minimized.

The design of the sapphire body is optimized to reduce the number of required processing steps, so that machining the raw material becomes more practical. Specifically, to avoid difficult and expensive machining of threads in bulk sapphire, we elected instead to glue threaded sleeves made of molybdenum into corresponding smooth bores.

Features of the STM head include a coarse approach motor built according to the design by S. H. Pan, a capacitive distance sensor<sup>13</sup> and a sample exchange mechanism. The

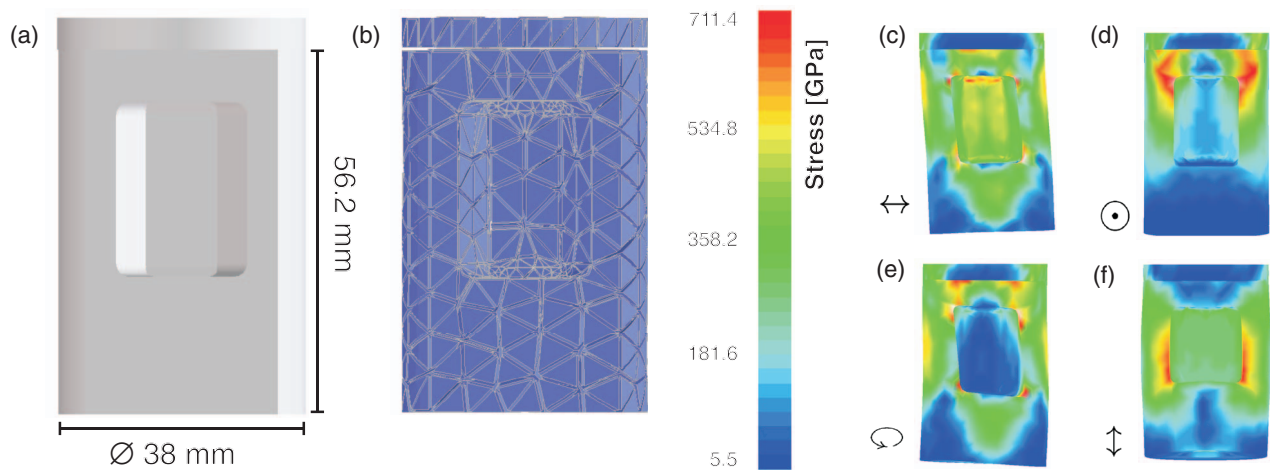


FIG. 1. (Color online) (a) 3D rendering of the main body of the STM head. (b) Mesh used for finite element analysis. (c)–(f) Fundamental modes of the STM head (fixed at the top) in the same order as the frequencies in Table I. (c) and (d) correspond to bending modes ( $\leftrightarrow$  and  $\odot$ ), (e) to a torsional mode ( $\odot$ ), and (f) to a longitudinal mode along the long axis of the body ( $\updownarrow$ ), which causes the strongest stress around the edges of the central cavity, as indicated by the color scale.

coarse approach piezos<sup>14</sup> are driven individually by a home-built piezo motor controller (PMC). This PMC drives slider movement in a frictional “walking mode,” in which the six piezo stacks are fired synchronously during the slow ramp, while the fast ramp is performed asynchronously – the piezos are actuated one at a time. This mode contrasts with inertial operation, or “jumping mode,” in which the six piezo stacks are always actuated synchronously. While the inertial mode simplifies the wiring – reducing the seven wires needed to connect the piezo motor to the electronics to two – it moves the slider less reliably. Operating the piezos in frictional or “walking mode” can increase the step size for the same driving voltage by up to a factor of two.<sup>15</sup>

Fig. 2(a) shows a computer aided design (CAD) rendering and Fig. 2(b) shows a photograph of the assembled STM

head. The relevant structural and functional components are labeled.

In order to operate the STM head in a cryogenic environment, we built a vacuum insert<sup>16</sup> which can be mounted in a commercial vapor shielded magnet dewar.<sup>17</sup> Our dewar has a 14 T (16 T with lambda stage) magnet with a 2 in. ( $\approx 50$  mm) cold bore and provides a holding time at base temperature of  $\sim 100$  h. To achieve operation at temperatures below 4.2 K, the insert is equipped with a 1 K pot which is continuously fed from the LHe bath via a thin capillary.<sup>19</sup> Operation of the 1 K pot does not affect the hold time of the dewar perceptively. To avoid additional noise production from the operation of the 1 K pot,<sup>20–22</sup> we have implemented pre-cooling measures to ensure that incoming LHe is cooled – ideally below the  $\lambda$ -point at 2.18 K – prior to entering the 1 K pot. The capillary that feeds the 1 K pot from the helium bath is  $\sim 1$  m long and has an inner diameter of  $100 \mu\text{m}$ . Pre-cooling is realized through thermal anchoring of the capillary to the outside of the 1 K pot along approximately half of its length – via coiling and soft soldering.

TABLE I. Comparison of fundamental mode frequencies (given in Hz) for different choices of material. Listed are the four lowest frequency modes. Finite element calculations were performed with the upper end of the STM head rigidly fixed, as it is in the experimental setup. The first two modes correspond to horizontal ( $\leftrightarrow$  and  $\odot$ ) bending of the body, the third to twisting ( $\odot$ ), and the fourth to asymmetric vertical ( $\updownarrow$ ) distortion. The simulated body and the corresponding mesh used are shown in Fig. 1. In addition, the density  $\rho$ , shear modulus  $G$ , Young’s modulus  $E$ , and the thermal conductivity at room temperature  $\kappa(300 \text{ K})$  are listed (values for MACOR from Ref. 38,  $\text{Al}_2\text{O}_3$  from Ref. 11, and sapphire from Ref. 39; isotropic averages were used which do not account for material anisotropy).

Modes [Hz]	Materials		
	MACOR	$\text{Al}_2\text{O}_3$	Sapphire
$\nu_1$	5264	7055	8488
$\nu_2$	5541	7323	8737
$\nu_3$	10 982	14 962	17 987
$\nu_4$	19 239	26 036	31 530
$\rho$ [ $\text{g}/\text{cm}^3$ ]	2.5	3.9	3.98
$G$ [GPa]	25.9	84.8	148.0
$E$ [GPa]	66.9	206.8	335.0
$\kappa(300 \text{ K})$ [ $\frac{\text{W}}{\text{m K}}$ ]	1.46	23	34–35.1

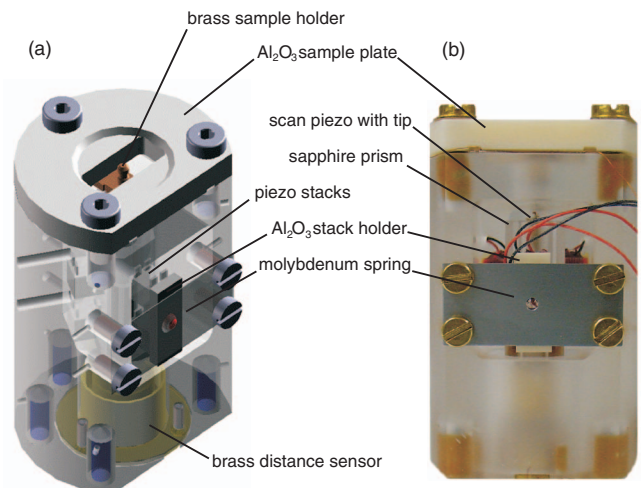


FIG. 2. (Color online) (a) CAD rendering of the assembled STM head. (b) Photograph of the STM head.

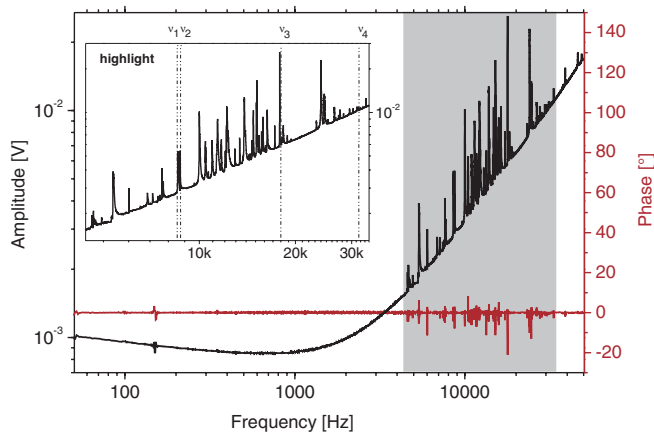


FIG. 3. (Color online) Sapphire STM head modes measured *in situ* with a lock-in amplifier, coarse approach piezo stacks are used for excitation (1 V) and response detection. The highlighted area is zoomed for a more detailed view; calculated positions of the four primary modes of the bare body (as listed in Table I) are denoted.

Figure 3 shows an *in situ* measurement of the response of the STM head to vibrational excitation via one of the piezo stacks. The measurements were performed on the fully assembled STM head (as shown in Fig. 2(b)) mounted in the dewar and at low temperature. The aberrations at 50, 100, and 150 Hz are artifacts due to the ac line frequency. Resonant modes begin to appear at frequencies higher than  $\sim 4.6$  kHz, with the first large peak appearing at 4.659 kHz.

Of course, other parts within the STM, such as the tip, scan piezo, and wiring, can have resonances of lower frequency which affect the stability of the tunneling junction. These modes do not show up in Fig. 3, however, because they do not excite the STM body. In order to minimize vibrational coupling to the tunnel junction due to wiring, our tip wire is thin and has been tightly bound to the sapphire body with Teflon tape.

Figure 4 shows a measurement of tunnel junction noise up to 200 Hz and the effects on noise of pumping on the 1 K-pot. It can be seen that for frequencies above 30 Hz, the curves measured with and without pumping of the 1 K-pot coincide; only for lower frequencies do differences emerge. We do not observe a degradation in the tunneling signal (either in topographies or in spectroscopy) due to operation of the 1 K pot. Also shown is the noise on the vibration table measured with a geophone.

The insert normally operates at a base temperature of down to  $\sim 1.2$  K (1 K plate) and 1.7 K (STM base plate), as measured by Cernox temperature sensors installed at these locations.<sup>23,24</sup> When the 1 K pot is not in operation, the temperature of the insert stabilizes at 4.2 K – the 1 K plate is then coupled via helium gas in the 1 K pot pump line to the helium bath.

The insert has a line-of-sight port, used for sample transfer, which begins at room temperature and ends at the measurement head at the center of the magnet. Along the way, there is a supporting structure (4 K plate) with a cleaving stage that allows for *in situ* sample cleaving in cryogenic vacuum and at low temperatures, and which at the same time acts as a radiation shield. A resistive heater mounted near the STM

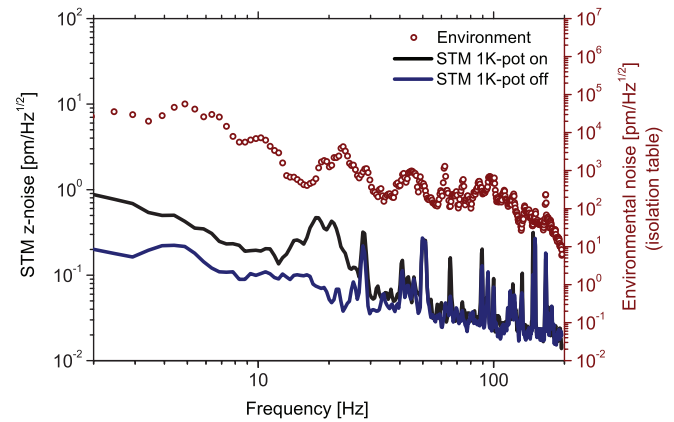


FIG. 4. (Color online) Tunnel junction noise at 1.8 K, with the 1K-pot turned on and off (i.e., being pumped or not pumped), as measured via the feedback loop control voltage applied to the scan piezo during tunneling. For comparison, the environmental noise on top of the isolation table was measured with a commercial geophone<sup>18</sup> and plotted alongside.

head expands the temperature range in which the instrument can be operated to  $\sim 1.7$ –20 K.

Our cryostat is mounted on a two-stage vibration isolation system. The outer stage consists of an  $\sim 7$  t concrete block, supported by steel springs, resting on the foundation of the building. The second stage consists of an  $\sim 1$  t vibration table, supported by a set of four pneumatic air springs,<sup>25</sup> resting on the concrete block. The cryostat is supported solely by the vibration table, but its center of mass and most of its length rest within a  $\varnothing = 60$  cm full-length bore in the concrete block.

The scanning element (5-pole piezo tube)<sup>26</sup> of the STM is controlled by a home-built high voltage amplifier with digitally controlled gains for movement in the  $x$ ,  $y$ , and  $z$  directions. Each direction is further subdivided into offset and scan channels, each with its own gain. This separation allows permanent access to the full range of scan piezo movement, even for small scan channel gain settings. The STM is controlled by the open source STM software GXSM (Refs. 27 and 28) and an open source scanning probe microscope controller.<sup>29</sup> The software has been modified for spectroscopic imaging functionality. The tunneling current is measured by a commercial current amplifier<sup>30</sup> with variable gain, which is also controlled by the integrated STM software.

Figure 5(a) shows first results obtained on *in situ* cleaved NbSe<sub>2</sub>. Atomic resolution and the charge density wave (CDW) order<sup>31</sup> can be seen easily. Figure 5(b) shows an image recorded (with a different STM tip) during operation of the 1 K pot. The line cuts in Figs. 5(c) and 5(d) allow us to estimate the residual vertical noise, which is below 1 pm under optimal conditions at 4.2 K, and also in the image taken at 1.7 K.

In order to estimate the energy resolution of our STM, we measured tunneling spectra as a function of temperature on NbSe<sub>2</sub>. The superconducting gap of NbSe<sub>2</sub> was first measured with scanning tunneling spectroscopy by Hess *et al.*<sup>32</sup> Due to the anisotropic band structure and coexistence with a CDW, the precise shape of the expected gap is not entirely clear (see, e.g., Refs. 33 and 34, and references therein).

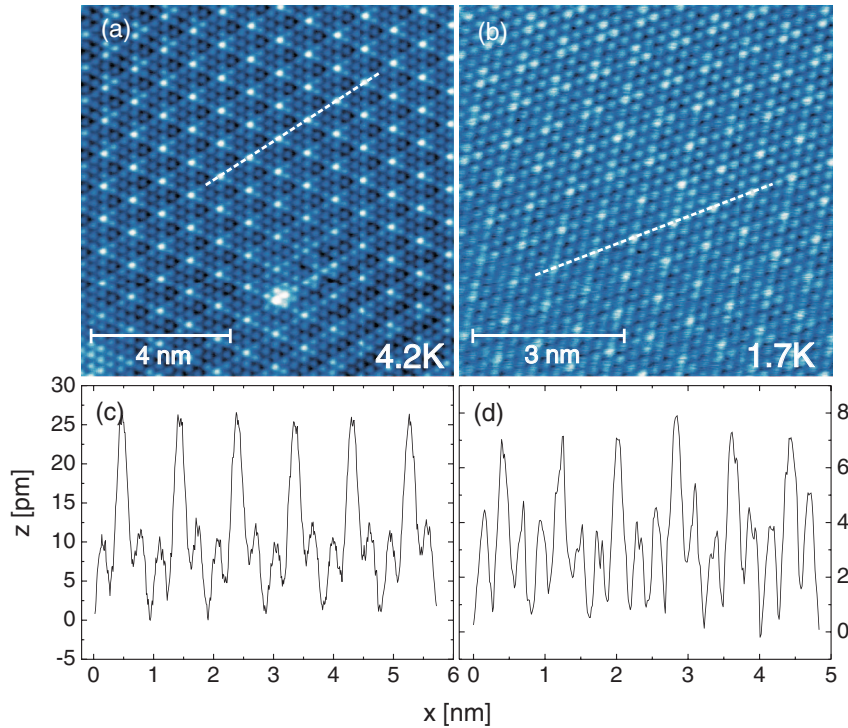


FIG. 5. (Color online) Topographic images (raw data) of NbSe<sub>2</sub> at (a) 4.2 K and (b) 1.7 K (while operating the 1 K pot) acquired with  $V = 100$  mV and  $I = 0.5$  nA, taken with different tips on different samples. (c) and (d) show line cuts through the topographic images in (a) and (b) along the indicated paths, demonstrating the vertical stability of the system.

Figure 6(a) shows tunneling spectra acquired on NbSe<sub>2</sub> at 4.2 K, 3 K (under temperature control<sup>35</sup>), and 1.7 K. The superconducting gap can be seen clearly. The temperature dependence indicates that the energy resolution achieved by the STM is sufficient to clearly differentiate gap features at 1.7 K from those measured at 4.2 K. Figure 6(b) shows calculated spectra for comparison. The calculated spectra were obtained by assuming that the superconducting gap in NbSe<sub>2</sub> can be described by the Dynes gap equation<sup>36</sup>

$$\rho(E) = \text{Re} \frac{E - i\Gamma}{\sqrt{(E - i\Gamma)^2 - \Delta^2}}, \quad (1)$$

using  $\Gamma = 120 \mu\text{V}$  and  $\Delta = 1.2$  mV. The spectra were obtained by first calculating the current,<sup>37</sup> taking into account the broadening due to the Fermi-Dirac-distribution. Thereafter, the differential conductance was obtained by calculating the lock-in derivative. We note that the real structure of the superconducting gap in NbSe<sub>2</sub> is more complex due to the aforementioned coexistence of CDW order with superconductivity and possible multiple gaps. This comparison can, therefore, only serve as an indication for the energy resolution of our instrument.

In conclusion, we have built a new measurement head for STM based on an improved design in which the materials

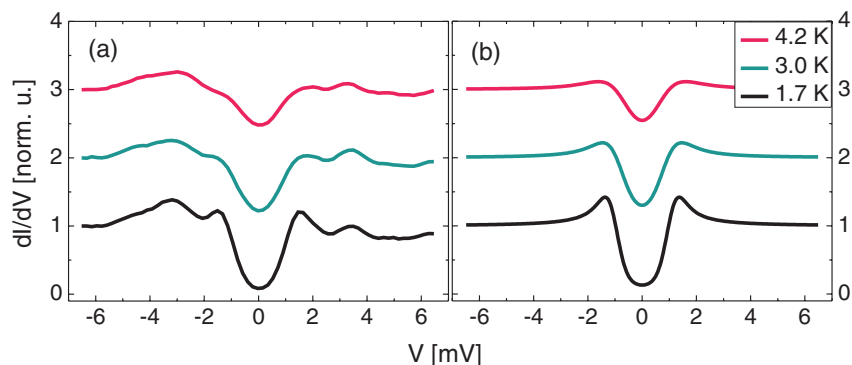


FIG. 6. (Color online) Tunneling spectroscopy characterization of NbSe<sub>2</sub>, revealing the superconducting gap. (a) Superconducting gap as a function of temperature (lock-in modulation: 0.5 mV, 405 Hz, 30 ms lock-in averaging); spectra are averaged from small maps. (b) Spectra calculated using Eq. (1) with the lock-in broadening used in the experiment. Spectra in (a) and (b) are normalized and spread out vertically for clarity.

are tuned for optimal vibrational stability and thermal conductivity, without introducing potential magnetic or electrical vulnerabilities. First measurement results demonstrating operation at low temperatures are shown.

We acknowledge support from the DFG through the priority program SPP1458. U.R.S. acknowledges support from the Alexander-von-Humboldt foundation.

- <sup>1</sup>Ø. Fischer, M. Kugler, I. Maggio-Aprile, and C. Berthod, *Rev. Mod. Phys.* **79**, 353 (2007).
- <sup>2</sup>K. McElroy, R. W. Simmonds, J. E. Hoffman, D.-H. Lee, J. Orenstein, H. Eisaki, S. Uchida, and J. C. Davis, *Nature (London)* **422**, 592 (2003).
- <sup>3</sup>A. R. Schmidt, M. H. Hamidian, P. Wahl, F. Meier, A. V. Balatsky, J. D. Garrett, T. J. Williams, G. M. Luke, and J. C. Davis, *Nature (London)* **465**, 570 (2010).
- <sup>4</sup>Y. Kohsaka, C. Taylor, P. Wahl, A. Schmidt, J. Lee, K. Fujita, J. W. Alldredge, J. Lee, K. McElroy, H. Eisaki, S. Uchida, D.-H. Lee, and J. C. Davis, *Nature (London)* **454**, 1072 (2008).
- <sup>5</sup>D. Pohl, *IBM J. Res. Dev.* **30**, 417 (1986).
- <sup>6</sup>S. Park and R. C. Barrett, "Design Considerations for an STM System," in *Scanning Tunneling Microscopy*, edited by J. A. Stroscio and W. J. Kaiser (Academic Press, San Diego, 1993); S. Park and R. C. Barrett, *Methods Exp. Phys.* **27**, 31 (1993).
- <sup>7</sup>C. R. Ast, M. Assig, A. Ast, and K. Kern, *Rev. Sci. Instrum.* **79**, 093704 (2008).
- <sup>8</sup>S. H. Pan, E. W. Hudson, and J. C. Davis, *Rev. Sci. Instrum.* **70**, 1459 (1999).
- <sup>9</sup>S. H. Pan, Piezoelectric motor, International Patent Publication No. WO 93/19494, International Bureau, World Intellectual Property Organization. A brief description of this device can be found in Refs. **8** and **10**.
- <sup>10</sup>C. Wittneven, R. Dombrowski, S. H. Pan, and R. Wiesendanger, *Rev. Sci. Instrum.* **68**, 3806 (1997).
- <sup>11</sup>FEM was done with the finite element modeling module, CoCreate Modeling v. 16.0.0.712, internal database.
- <sup>12</sup>The relative difference in thermal conductivity between sapphire and granular Al<sub>2</sub>O<sub>3</sub> grows significantly between 300 K and cryogenic temperatures, from about 1.5 up to ~100 times higher; see also J. W. Ekin, *Experimental Techniques for Low Temperature Measurements* (Oxford University Press, New York, 2006).
- <sup>13</sup>J. E. Hoffman, Ph.D. dissertation, University of California, Berkeley, 2003.
- <sup>14</sup>Piezo stacks P-121.03 from Physik Instrumente Ceramic GmbH.
- <sup>15</sup>G. Mariotto, M. D'Angelo, and I. V. Shvets, *Rev. Sci. Instrum.* **70**, 3651 (1999).
- <sup>16</sup>E. T. Swartz, *Rev. Sci. Instrum.* **57**, 2848 (1986).
- <sup>17</sup>Vapour shielded helium dewar by Oxford Instruments with a 14 T magnet (up to 16 T with lambda cooling).
- <sup>18</sup>SeisMonitor by Oyo Geospace, Houston, TX.
- <sup>19</sup>CuNi capillary from GVL Cryoengineering.
- <sup>20</sup>A. Raccanelli, L. A. Reichertz, and E. Kreysa, *Cryogenics* **41**, 763 (2001).
- <sup>21</sup>P. Gorla, C. Bucci, and S. Pirro, *Nucl. Instrum. Methods Phys. Res. A* **520**, 641 (2004).
- <sup>22</sup>G. Lawes, G. M. Zassenhaus, S. Koch, E. N. Smith, J. D. Reppy, and J. M. Parpia, *Rev. Sci. Instrum.* **69**, 4176 (1998).
- <sup>23</sup>Cernox 1030SD and 1050SD sensors from LakeShore Cryotronics, Inc.
- <sup>24</sup>LakeShore temperature controller 336 from Cryophysics GmbH.
- <sup>25</sup>External passive vibration isolation system I-2000-410 from Newport Spectra-Physics GmbH.
- <sup>26</sup>Scan piezo tube element #4 from EBL Products Inc.
- <sup>27</sup>P. Zahl, M. Bierkandt, S. Schröder, and A. Klust, *Rev. Sci. Instrum.* **74**, 1222 (2003).
- <sup>28</sup>P. Zahl, T. Wagner, R. Möller, and A. Klust, *J. Vac. Sci. Technol. B* **28**, C4E39 (2010).
- <sup>29</sup>Soft dB Inc., Québec, Canada; see <http://www.softdb.com>.
- <sup>30</sup>Variable gain current amplifier FEMTO Messtechnik GmbH DLPCA-200.
- <sup>31</sup>B. Giambattista, A. Johnson, R. V. Coleman, B. Drake, and P. K. Hansma, *Phys. Rev. B* **37**, 2742 (1988).
- <sup>32</sup>H. F. Hess, R. B. Robinson, R. C. Dynes, J. M. Valles, Jr., and J. V. Waszczak, *Phys. Rev. Lett.* **62**, 214 (1989).
- <sup>33</sup>Y. Noat, T. Cren, F. Debontridder, D. Roditchev, W. Sacks, P. Toulemonde, and A. San Miguel, *Phys. Rev. B* **82**, 014531 (2010).
- <sup>34</sup>I. Guillamon, H. Suderow, F. Guinea, and S. Vieira, *Phys. Rev. B* **77**, 134505 (2008).
- <sup>35</sup>Lakeshore Model 336 temperature controller.
- <sup>36</sup>R. C. Dynes, V. Narayanamurti, and J. P. Garno, *Phys. Rev. Lett.* **41**, 1509 (1978).
- <sup>37</sup>N. D. Lang, *Phys. Rev. B* **34**, 5947 (1986).
- <sup>38</sup>Data sheet for MACOR by Corning Incorporated Lighting&Materials, Corning, New York.
- <sup>39</sup>Frank Träger, *Springer Handbook of Lasers and Optics* (Springer, New York, 2007).